

PROCEEDINGS OF SPIE

SPIDigitalLibrary.org/conference-proceedings-of-spie

The presence and location of podocytes in glomeruli as affected by diabetes mellitus

Kathryn Maraszek, Briana Santo, Rabi Yacoub, John Tomaszewski, Imtiaz Mohammad, et al.

Kathryn E. Maraszek, Briana A. Santo, Rabi Yacoub, John E. Tomaszewski, Imtiaz Mohammad, Amber M. Worrall, Pinaki Sarder, "The presence and location of podocytes in glomeruli as affected by diabetes mellitus," Proc. SPIE 11320, Medical Imaging 2020: Digital Pathology, 1132018 (16 March 2020); doi: 10.1117/12.2548904

SPIE.

Event: SPIE Medical Imaging, 2020, Houston, Texas, United States

The Presence and Location of Podocytes in Glomeruli as Affected by Diabetes Mellitus

Kathryn E. Maraszek^{1, *}, Briana A. Santo^{1, *}, Rabi Yacoub², John E. Tomaszewski¹,
Imtiaz Mohammad¹, Amber M. Worral¹, Pinaki Sarder^{1, **}

¹Department of Pathology and Anatomical Sciences

²Medicine – Nephrology

University at Buffalo – The State University of New York

*Signifies equal contribution

**Address all correspondence to: Pinaki Sarder

Tel: 716-829-2265; E-mail: pinakisa@buffalo.edu

ABSTRACT

The primary purpose of the kidney, specifically the glomerulus, is filtration. Filtration is accomplished through the glomerular filtration barrier, which consists of the fenestrated endothelium, glomerular basement membrane, and specialized epithelial cells called podocytes. In pathologic states, such as Diabetes Mellitus (DM) and diabetic kidney disease (DKD), variable glomerular conditions result in podocyte injury and depletion, followed by progressive glomerular injury and DKD progression. In this work we quantified glomerulus and podocyte structural changes in histopathology image data derived from a murine model of DM. Using a variety of image processing techniques, we studied changes in podocyte morphology and intra-glomerular distribution across healthy, mild DM, and DM glomeruli. Our feature analysis provided feature trends which we believe are reflective of DKD pathology; while glomerular area peaked in mild DM, average podocyte number and distance from the urinary pole continued to decrease and increase, respectively, throughout DM. Ultimately, this study aims to augment the set of quantifiable image biomarkers used for evaluation of DKD progression in digital pathology, as well as underscore the importance of engineering biologically-inspired image features.

Key-words (5): Diabetes Mellitus, Podocyte, Glomerular filtration barrier, Feature engineering, Image analysis

1. INTRODUCTION

The primary function of the kidney is to filter waste out of blood. This is in part accomplished through the structural unit known as the glomerulus, and its filtration barrier, which reside within the nephron. The glomerular filtration barrier (GFB) is comprised of the fenestrated endothelium, glomerular basement membrane, and specialized epithelial cells called podocytes¹. Podocytes possess tentacle-like structures known as foot processes that interdigitate to form specialized intercellular junctions known as slit diaphragms (SDs). Podocyte SDs facilitate selective filtration of molecules and solutes through the GFB². In pathologic states, such as diabetic kidney disease (DKD), changing glomerular conditions³ result in podocyte injury and depletion. More specifically, the marked increase in glomerular filtration pressure (GFP) results in glomerulomegaly⁴, as well as podocyte shear stress, effacement, and eventual shedding from the GFB⁵. Podocyte injury and depletion compromise GFB integrity and effective glomerular filtration², allowing harmful substances to pass into the surrounding urinary space and incite global, glomerular injury. Cumulative glomerular injury facilitates DKD progression and eventual kidney failure^{3, 6}. According to recent research, Diabetes Mellitus (DM) is one of the leading causes of kidney failure in the United States⁷. In fact, the International Diabetes Foundation predicts that approximately 439 million people will have Diabetes in 2030, which represents an increase of approximately 50% from 2010². Given the increasing incidence of DM, there is an anticipated increase in DKD and the volume of patients progressing to kidney failure⁸. Therefore, elucidation of the exact mechanisms governing DKD progression, from podocyte injury and depletion, to GFB denudation and global, glomerular injury, is paramount to development of interventional strategies and disease prevention.

Methods for evaluating podocyte injury and depletion include quantification of podocytes in digital renal pathology⁹. Such methods involve computation of image features indicative of podocyte textural and morphological change in healthy and disease states. Given that podocyte shear stress and depletion are implicated in disease progression, we proposed a novel image feature which quantifies podocyte intra-glomerular distribution. More specifically, we engineered a feature which quantifies podocyte proximity to the urinary pole (UP) – the junction between the glomerulus capsule and proximal convoluted tubule⁵. Podocyte shear force and stress are greatest at this location⁵, and UP-proximal podocytes are the most likely to incur injury and be shed in disease states. Therefore, the average Euclidean distance of podocytes from the UP should reflect this biological phenomena, providing a larger average distance in disease. To explore the implications of this handcrafted feature, we derived a large set of glomerulus images a mouse model emulating DKD¹⁰ (streptozotocin (STZ) – induced diabetic model) and computed a variety of podocyte, nuclear, and glomerular indicative of DM-related change as a point of comparison.

2. METHODS

2.1 Murine data. A murine model emulating diabetic-kidney disease (diabetes mellitus, DM) was selected for this study. For murine model details, see our earlier publication¹¹. All animal studies were performed in accordance with protocols approved by the Institutional Animal Care and Use Committee at University at Buffalo, are consistent with federal guidelines and regulations, and are in accordance with recommendations of the American Veterinary Medical Association guidelines on euthanasia. Control ($n = 7$) and disease ($n = 3$ mild DM, $n = 4$ DM) kidney tissues (Table 1) were gathered, formalin fixed and paraffin embedded, sectioned (2 μ m, sagittal plane), and mounted on glass slides.

2.2 Immunofluorescence (IF) staining and imaging: Tissue sections were labeled using Wilms Tumor 1 (WT 1) (Abcam, ab89901) as a primary antibody with Alexa Fluor 594 (Abcam, ab 150129, ex/em (nm): 495/519) as the secondary. Tissue sections were spotted with DAPI mounting media (Vectashield Antifade Mounting Medium with DAPI, ex/em (nm): 358/461, Vector Laboratories, Inc) and coverslips were applied. Slides were stored for the duration at 4°C. A whole-slide fluorescence microscope (Aperio Versa, 40X, NA = 1.4, Nuance EX Multispectral Imaging Camera, Leica Microsystems, Buffalo Grove, IL) was used to capture red/green/blue (RGB) whole slide images (WSIs). The completed sample preparation and staining procedure was consistent with existing protocols for IF staining in FFPE tissues.

2.3 Histology (PAS) post-staining and imaging: After IF whole slide imaging, tissues were post-stained with Periodic Acid-Schiff and a Hematoxylin counter-stain. The application of PAS post-stain required careful dissolution of mounting media and coverslip removal. Mounting media was dissolved via repeated immersion in xylene. With each immersion, the coverslip was gently and incrementally pulled back, preserving tissue integrity and orientation.

Tissue sections were then stained using PAS, and bright field (BF) WSIs were captured using a whole-slide scanner (Aperio ScanScope, 40X, Leica Microsystems, Buffalo Grove, IL).

Mouse ID	Disease Status	Glomerulus Images	UP Annotations
P1	Mild DM	59	19
P2	Mild DM	74	29
P3	Mild DM	59	18
P4	DM	93	18
P5	DM	60	16
P12	DM	24	7
P15	DM	58	21
P16	Control	47	19
P18	Control	80	34
P19	Control	51	12
P20	Control	48	11
P21	Control	77	14
P24	Control	44	11
P25	Control	109	19
Total	-	883	248

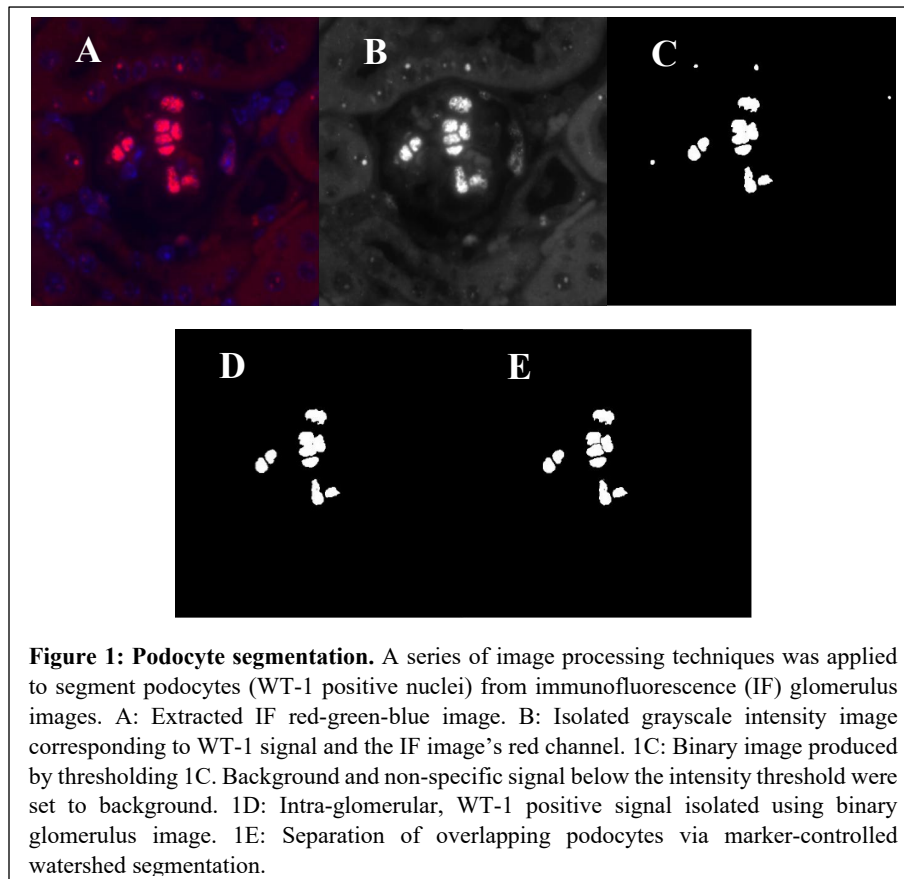
Table 1: Summary of murine data. A total of 14 mice were used for this study including 7 control, 3 mild DM, and 4 DM. The quantity of glomerulus images per mouse is provided, as well as the quantity of glomerulus images featuring the urinary pole (UP) within the plane of section. All glomerulus images featuring a UP were annotated.

2.4 PAS Glomerulus segmentation: Glomeruli were manually annotated in a subset ($n = 3$) of PAS WSIs using Aperio ImageScope. Manual annotations were used to train our lab's published H-AI-L tool¹²: a convolutional neural network (CNN) developed for automated segmentation of glomeruli from BF WSIs. After network training, H-AI-L was enlisted to predict glomerulus boundaries in the remaining ($n = 11$) PAS WSIs. Images of glomeruli were subsequently extracted from BF WSIs. Binary masks of each glomerulus image were also produced, with the glomerulus unit set to foreground. Glomerulus coordinates were also derived from segmented regions.

2.5 Urinary Pole Annotation: The urinary pole (UP), described as the junction between the glomerulus (Bowman's) capsule and the proximal convoluted tubule⁵, was identified in a subset of PAS images by experienced digital pathology annotators. Table 1 provides the quantity of glomerulus images wherein the UP was readily discernible and within the plane of the tissue section. UPs were annotated in green on each respective image. Annotations were saved as a separate binary image for later use.

2.6 IF Glomerulus extraction and annotation: To extract each glomerulus from the corresponding IF WSI, glomerulus coordinates were rescaled and translated according to the dimensions and resolutions of the BF and IF WSIs. IF images were then split into R, G, and B grayscale intensity images. While WT-1 and DAPI occupied the red and blue channels, respectively, the green channel featured no information relevant to the task at hand. Therefore, the UP annotation image was assigned to the green channel.

2.7 IF Podocyte segmentation: Within the glomerulus, WT-1 immunostaining provides for the labeling and detection of podocyte nuclei¹³. For brevity, WT-1 positive podocyte nuclei will be referred to as podocytes hereafter. To segment podocytes, a binary image corresponding to specific WT-1 signal was generated (Figure 1C) by thresholding the red channel's grayscale intensity image (Figure 1B). The threshold value was automatically computed for each image as the mean pixel intensity value. Intra-glomerular WT-1 signal was specified by logically combining this podocyte binary image with the binary glomerulus image derived via H-AI-L¹⁴. The result was a logical mask of intra-glomerular, WT-1 positive signal exclusively. This logical mask was then refined via a series of morphological image processing techniques¹⁵ including size exclusion and morphological opening, to provide a preliminary podocyte mask (Figure 1D). Marker-controlled watershed segmentation¹⁶ was then applied to separate overlapping podocytes (Figure 1E). Glomerulus images from a subset of WSIs ($n = 6$, 2 each of control, mild DM, and DM) were randomly selected and podocytes were manually annotated as ground truth. Ground truth annotations were later enlisted for evaluation of podocyte segmentation performance.



2.8 IF Podocyte Feature Engineering: Podocyte nuclei were enumerated, and each nucleus' morphological and intensity features were derived including: area, eccentricity, solidity, pixel intensity statistics, and centroid location. Derivation of these features was achieved via application of MATLAB *regionprops*. Additional engineered features included mean podocyte proximity to the urinary pole. This metric was computed by taking each podocyte's centroid location and calculating the Euclidean distance between each centroid and the central point of the urinary pole annotation. Distance- and area-based features were converted to microns (μm , μm^2) to place measurements within biological context. All features were recorded for subsequent statistical analysis.

2.9 IF Nuclei segmentation: Within the glomerulus, DAPI counterstaining provides for the labeling and detection of all DNA-rich regions¹⁷. More specifically, the DAPI counterstain binds to the A and T (adenine-thymine) DNA base

pairs illuminating all nuclear regions. To segment nuclei, a logical mask corresponding to specific DAPI signal was generated by thresholding the blue channel's grayscale intensity image. The threshold was automatically computed for each image as the mean pixel intensity value. The logical mask was then refined via a series of morphological image processing techniques including size exclusion and morphological opening, to provide a preliminary nuclei mask. Marker-controlled watershed segmentation¹⁶ was then applied in order to separate overlapping nuclei. Glomerulus images from a subset of WSIs ($n = 6$, 2 each of control, mild DM, and DM) were randomly selected and nuclei were manually annotated as ground truth. Ground truth annotations were later enlisted for evaluation of nuclear segmentation performance.

2.10 Collective Nuclear and Glomerulus Feature Engineering: Intra-glomerular nuclei were enumerated, and each nucleus' morphological and intensity features were derived including: area, eccentricity, solidity, pixel intensity statistics, and centroid location. Derivation of these features was achieved via application of MATLAB *regionprops*. In addition, feature ratios were computed for all aforementioned features in order to compare the podocyte and collective nuclei within each glomerulus unit. Glomerular features were also derived including: area, perimeter, eccentricity, and solidity. Distance- and area-based features were converted to microns (μm , μm^2) to place measurements within biological context. All features were recorded for subsequent statistical analysis.

2.11 Comparison of control and disease murine histomorphology: Feature-based comparison of control and disease podocyte, nuclear, and glomerulus morphological phenotypes was completed to determine whether our quantified image features enable discrimination of disease status.

3. RESULTS

3.1 Immunofluorescence (IF) staining and imaging: When previewed under a microscope, control slides stained with IF probes featured no specific-signal, while experimental slides featured specific signal. These results are consistent with immunofluorescence staining protocols, which involve the application of primary antibody (prepared in blocking solution) to experimental slides exclusively. Control slides are instead treated with blocking solution. Co-author and expert histotechnologist Dr. Imtiaz Mohammad confirmed the successful application of immunostaining in experimental slides. As imaging experts, co-author Dr. Amber Worral and corresponding author Dr. Pinaki Sarder confirmed the quality of acquired IF WSIs.

3.2 Histology (PAS) post-staining and imaging: When previewed under a microscope, tissue regions expected to stain PAS- and hematoxylin- positive, basement membranes and nuclei respectively, presented with quality staining. This observation, made by co-author and expert histotechnologist Dr. Imtiaz Mohammad, confirmed the successful application of histology stains. Similarly, co-author Dr. Amber Worral and corresponding author Dr. Pinaki Sarder confirmed the quality of acquired BF WSIs.

3.3 PAS Glomerulus segmentation: Performance metrics for the base H-AI-L model, provided as an open source application, are detailed in Lutnick *et al.*'s recent publication¹². A total of $n = 883$ glomerulus images were extracted across all BF WSIs (Table 1).

3.4 IF Glomerulus extraction and annotation: For each PAS glomerulus image, the corresponding IF image was acquired (e.g. Figure 1A). In addition, all IF images corresponding to PAS images with a visible UP ($n = 248$) featured the rescaled UP annotation (Table 1).

3.5 IF Podocyte segmentation: Podocyte ground truth annotations were converted to binary images with podocytes set to foreground. Pixel-wise comparison of ground truth and pipeline podocyte segmentation were performed, and the following performance metrics were computed: Sensitivity = 0.727, Specificity = 0.999, Accuracy = 0.959. (Table 2). These metrics underscore the quality of our podocyte segmentation. We believe that computed sensitivity is low due to the nature of ground truth generation, wherein WT-1 positive nuclei were manually annotated. In an IF image, the signal intensity at the boundary of labeled podocytes is less distinct to the eye than signal-dense intra-nuclear

regions. Therefore, exact annotation of the boundary is challenging.

3.6 IF Nuclei segmentation: Nuclear ground truth annotations were converted to binary images with nuclei set to foreground. Pixel-wise comparison of ground truth and pipeline podocyte segmentation were performed, and the following performance metrics were computed: Sensitivity = 0.771, Specificity = 0.997, Accuracy = 0.977 (Table 2). These metrics underscore the quality of our nuclear segmentation. We believe that computed sensitivity is low due to the nature of ground truth generation, wherein DAPI positive nuclei were manually annotated. In an IF image, the signal intensity at the boundary of labeled nuclei is less distinct than signal-dense intra-nuclear regions. Therefore, exact boundary annotation is challenging.

Computational Performance	Podocytes (WT-1)	Collective Nuclei (DAPI)
Sensitivity	0.727	0.771
Specificity	0.999	0.997
Accuracy	0.959	0.977

Table 2: Pipeline computational performance for podocytes and all nuclei. To evaluate the quality of our podocyte and nuclear segmentation, ground truth annotations were compared with pipeline output and the above statistics were computed.

3.7 IF Podocyte Feature Engineering: Podocytes were quantified in glomerulus images. Across all WSIs, podocyte populations averaged approximately 17 podocytes per glomerulus unit, but ranged anywhere from 10 to 24 (Table 3). Features derived for podocyte populations included: area, eccentricity, solidity, mean podocyte pixel intensity, and distance to urinary pole. The mean and standard deviation for each of the aforementioned features were computed across the intra-glomerular podocyte population, and subsequently across the WSI glomerulus population. All features were analyzed within the context of control, mild DM, and DM (Table 3).

3.7.1 Feature trends irrespective of disease status: Podocyte features were first analyzed independent of disease status (Table 3, “All” Column). Descriptive of morphology, computed eccentricity suggests that, collectively, podocytes are elliptical or elongated. In addition, with a mean solidity significantly less than one, podocytes feature a more irregular morphology including both concave and convex perimeter regions. For a given glomerulus, the average podocyte distance to the UP was 45 μm and the average pixel intensity was 161 (scale 0 - 255). The latter feature, average pixel intensity, provides a relative approximation of WT-1 signal intensity, and therefore WT-1 expression.

3.7.2 Feature trends with respect to disease status: Podocyte features were then analyzed within the context of disease status. It was found that as the severity of disease increased – from control to mild DM, and DM – the quantity of podocytes decreased, while the area and distance from the UP increased. The observed decrease in podocyte quantity was expected. Of particular interest was the relative proximity of podocytes to the UP, which is revisited in the glomerulus feature section and paper discussion. More severe disease status was also associated with a slight decrease in eccentricity and little-no change in solidity. Interestingly, the average pixel intensity increased slightly from control to Mild DM, and then dropped off significantly in DM. The sharp change in WT-1 signal intensity observed between Mild DM and DM suggests a change in podocyte WT-1 expression and phenotype.

3.8 Collective Nuclear and Glomerulus Feature Engineering: Nuclei were quantified in glomerulus images. Across all WSIs, intra-glomerular nuclear counts averaged approximately 46 nuclei, but ranged anywhere from 39 to 53 (Table 3). Features derived for nuclei included: area, eccentricity, solidity, mean nuclear pixel intensity, and distance to urinary pole. The mean and standard deviation for each of the aforementioned features were computed across the intra-glomerular nuclei population, and subsequently across the WSI glomerulus population. All features were analyzed within the context of control, mild DM, and DM (Table 3).

3.8.1 Feature trends irrespective of disease status: Nuclear and glomerulus features were first analyzed independent of disease status (Table 3, “All” Column). As expected, the average quantity of nuclei per glomerulus far exceeded that of podocytes. On average, podocytes accounted for approximately one third ($\approx 17/46$) of the intra-glomerular nucleus population. Similar to podocytes, computed eccentricity and solidity suggest that all nuclei deviate from circularity and concavity, although to a lesser extent. For a given glomerulus, the average nucleus distance to the UP was 50 μm and the average pixel intensity was 134 (scale

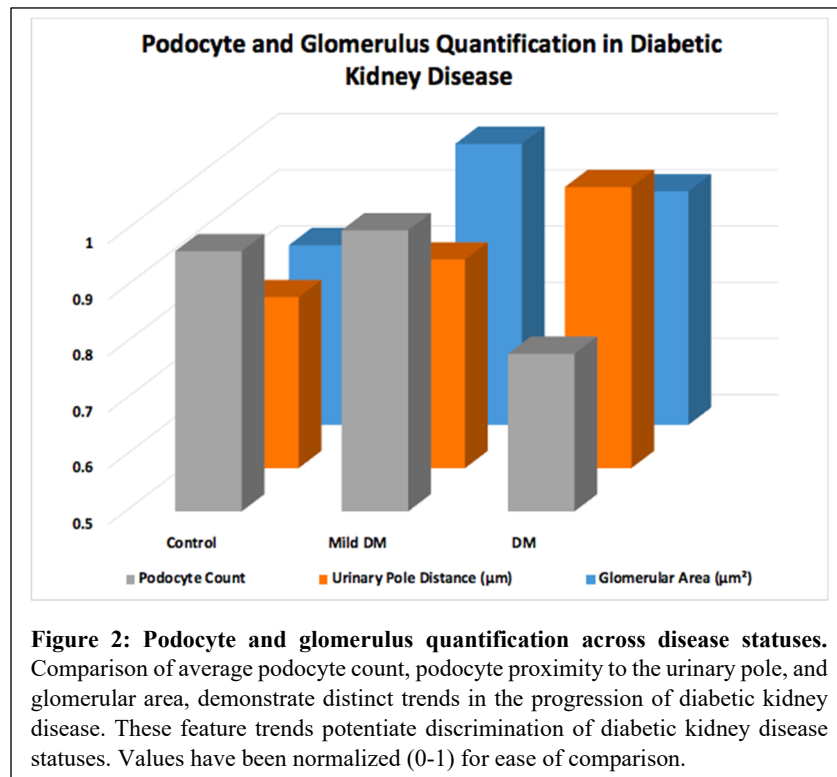
0 - 255). The latter feature, average pixel intensity, provides a relative approximation of DAPI signal intensity, and therefore DNA concentration. Murine tissue sections averaged 63 glomeruli, providing for a large image sample size per mouse. Glomerular area and perimeter averaged $6311 \mu\text{m}^2$ and $303 \mu\text{m}$, respectively. As expected, glomerular area far exceeded that of podocytes and all nuclei. On average, an individual podocyte accounted for $\cong 6\%$ of glomerular area. Similar to podocytes and all nuclei, glomerulus eccentricity deviated from circularity with a mean value of 0.556. Glomerulus morphology proved distinct in that the average solidity was 0.997. With a solidity approximating one, glomeruli are almost perfectly convex featuring little-no irregularity in their boundaries.

3.8.2 Feature trends with respect to disease status: Nuclear and glomerulus features were then analyzed within the context of disease status. It was found that a variety of computed features peaked in the mild DM disease state, and dropped off in DM. These features included average nuclear quantity and area, as well as average glomerular area and perimeter. We believe that this feature trend reflects the pathogenesis of diabetic kidney disease, further detailed in the discussion section. Compared to the aforementioned features, the average nuclear-UP distance and pixel intensity increased with disease severity – from control to mild DM, and DM – while the following features proved consistent: average nuclear and glomerular eccentricity and solidity.

Features	Control	Mild DM	DM	All
Podocyte Quantity	14.32 ± 3.03	14.88 ± 0.39	11.61 ± 2.07	13.82 ± 2.74
Area (μm^2)	23.92 ± 1.58	25.34 ± 0.59	10.60 ± 1.04	21.57 ± 0.84
Average Pixel Intensity	170.2 ± 4.86	179.0 ± 1.04	122.7 ± 9.21	161.3 ± 6.61
Eccentricity	0.701 ± 0.01	0.680 ± 0.02	0.663 ± 0.03	0.688 ± 0.03
Solidity	0.111 ± 0.01	0.096 ± 0.01	0.108 ± 0.02	0.107 ± 0.01
Urinary Pole Distance (UPD) (μm)	43.74 ± 3.07	45.53 ± 1.95	48.78 ± 3.23	45.32 ± 3.53
Collective Nuclear Quantity	43.12 ± 4.86	51.36 ± 1.04	46.47 ± 9.21	45.80 ± 6.61
Area (μm^2)	25.71 ± 2.82	26.01 ± 0.48	25.91 ± 5.33	25.83 ± 3.83
Average Pixel Intensity	133.0 ± 18.2	130.4 ± 11.4	139.5 ± 11.6	133.9 ± 15.8
Eccentricity	0.605 ± 0.01	0.595 ± 0.01	0.587 ± 0.01	0.599 ± 0.01
Solidity	0.216 ± 0.01	0.211 ± 0.01	0.211 ± 0.01	0.214 ± 0.01
Urinary Pole Distance (UPD) (μm)	48.10 ± 3.60	49.26 ± 0.54	54.55 ± 6.30	49.85 ± 4.80
Glomerulus Quantity	65.14 ± 22.5	64.00 ± 7.07	58.75 ± 24.4	63.07 ± 21.0
Area (μm^2)	5856 ± 534	7144 ± 383	6540 ± 999	6311 ± 838
Perimeter (μm)	292.8 ± 11.1	323.8 ± 8.89	307.0 ± 23.8	303.3 ± 19.4
Eccentricity	0.562 ± 0.02	0.563 ± 0.02	0.537 ± 0.01	0.556 ± 0.02
Solidity	$0.975 \pm .001$	$0.979 \pm .002$	$0.980 \pm .001$	$0.977 \pm .003$

Table 3: Podocyte, Collective Nuclear, and Glomerulus Features. Intensity refers to pixel intensity and reflects the relative intensity of immunofluorescence staining. All values are calculated as an average across glomerulus images. Distance and area features have been converted from pixels to microns (μm , μm^2) to put measurements within biological context. Error bar indicates standard deviation.

3.9 Comparison of control and disease murine histomorphology: Comparison of a subset of podocyte and glomerulus features across control, mild DM, and DM mice demonstrated distinct trends in the progression of diabetic kidney disease (Figure 2). Selected features for comparison included: podocyte count, podocyte proximity to the urinary pole – computed as the average podocyte distance from the UP – and glomerular area. While glomerular area increased drastically from control to mild DM, peaking at $\approx 7000+ \mu\text{m}^2$, before rapidly dropping off in DM, the average quantity and UP-distance of podocytes increased continuously. The distinct difference in feature values between control, mild DM, and DM, potentiates feature-based classification. In addition, the ability to discriminate between disease statuses via computed UP-distance emphasizes the value of this engineered feature.



4. DISCUSSION

Although popular areas of research, the podocyte depletion hypothesis^{6, 18} and the podocyte response to disease conditions (i.e. changes in glomerular filtration pressure⁵) remain indefinite. In this work, we capitalized upon immunofluorescence and histology staining in order to quantify podocyte morphology and spatial distribution as a function of disease severity. Despite the quality of our podocyte and nuclear segmentations, underscored by our computed performance metrics (Table 3), a few biological facts warrant further discussion within the context of our work. Podocytes may be binucleate^{9, 19}. Because our podocyte identification is based upon a nuclear marker (WT-1), should a binucleate podocyte be present, it will be counted as two independent cells. Additionally, parietal epithelial cells (PECs) are an alternative intra-glomerular cell which stain positively for WT-1²⁰. However, PEC expression of WT-1 manifests as petite, punctate signals whereas podocyte expression of WT-1 is diffuse. Therefore, our application of morphological processing techniques (e.g. size exclusion) during image segmentation eliminated PECs from quantification. Alternative application of an exclusive podocyte marker such as p57^{kip2} – a nuclear marker of terminal differentiation²¹ – would also prevent PEC detection and quantification. Regardless, we attribute the success of our podocyte and nuclear segmentations (Table 3) to the quality of immunostaining as well as the application of marker-controlled watershed segmentation (Figure 1E). This refined segmentation method provided for successful separation of overlapping podocytes and nuclei, avoiding the oversegmentation¹⁶ characteristic of traditional watershed segmentation based upon image gradient.

In this work we engineered a variety of features descriptive of podocyte, nuclear, and glomerular phenotype. While some features were readily derived via built-in MATLAB functions (e.g. area), others required ingenuity and customization (e.g. UP proximity). Visualization of select inter-feature relationships (Figure 2) revealed distinct features trends between disease states. As an established biomarker in diabetic kidney disease, variation in glomerular area^{4, 7, 22} allowed us to place podocyte number and UP-distance within the context of disease progression. Glomerular area increased drastically from control to mild DM, peaking at 7000+ μm^2 , before rapidly dropping off in DM. Referred to as glomerulomegaly²² in kidney pathology, this large increase in glomerular area is due to increased glomerular filtration pressure (GFP). Podocyte shear stress, shedding proximal to the UP⁵, and increased proliferation at the vascular pole²³ are attributed to this glomerular pathology. In addition, kidney pathology describes subsequent decrease in GFP and glomerular collapse³. We believe that our observed feature trends are reflective of this unique disease pathology; while glomerular area peaked in mild DM³, throughout DM average podocyte number progressively declined and average distance from the urinary pole continually increased. We emphasize the decrease in podocyte quantity, as this observation confirms that increasing podocyte-UP distance is not simply a product of glomerular diameter (area), but rather is indicative of podocyte loss proximal to the UP. Podocyte proximity to the UP is a biologically-inspired and informed feature potentiating discrimination of disease statuses that warrants further computational exploration.

5. CONCLUSION AND FUTURE WORK

Our work not only provides for automated, computational assessment of immune-labeled podocytes in *ex vivo* samples, but also potentiates a unique image feature in digital renal pathology: podocyte proximity to the urinary pole. Given that observed feature trends were reflective of established kidney pathology, we believe podocyte spatial distribution warrants further exploration. For example, computation of podocyte proximity to the vascular pole²³ (VP). In addition, our work emphasizes the value of engineered features inspired by biological knowledge. Although intensive, computation of biologically-informed features enables direct interpretation of results within biological context. This feature interpretability is preferred to the ambiguous, “black box” nature of machine extracted features²⁴⁻²⁶. Therefore, the focus of future work will be the engineering of additional, biologically-inspired features, as well as the development of a machine learning classifier (e.g. support vector machine, SVM) to evaluate the ability of engineered features to classify disease status.

6. ACKNOWLEDGEMENTS

The project was supported by the faculty startup funds from the Jacobs School of Medicine and Biomedical Sciences, University at Buffalo; Buffalo Blue Sky grant, University at Buffalo; NIDDK Diabetic Complications Consortium grant DK076169; NIDDK grant R01 DK114485 & DK114485 02S1; NIDDK CKD Biomarker Consortium grant U01 DK103225; and NIDDK Kidney Precision Medicine Project grant U2C DK114886. We acknowledge the assistance of the Multispectral Imaging Suite and Histology Core Laboratory in the Dept. of Pathology & Anatomical Sciences, Jacobs School of Medicine and Biomedical Sciences, University at Buffalo.

REFERENCES

- [1] J. Patrakka, K. J. B. Tryggvason, and b. r. communications, “Molecular make-up of the glomerular filtration barrier,” 396(1), 164-169 (2010).
- [2] H. Kawachi, N. Miyauchi, K. Suzuki *et al.*, “Role of podocyte slit diaphragm as a filtration barrier,” 11(4), 274-281 (2006).
- [3] T. W. C. Tervaert, A. L. Mooyaart, K. Amann *et al.*, “Pathologic classification of diabetic nephropathy,” CJASN, 21(4), 556-563 (2010).
- [4] G. J. C. d. r. Eknayan, “Obesity, diabetes, and chronic kidney disease,” 7(6), 449 (2007).
- [5] C. Friedrich, N. Endlich, W. Kriz *et al.*, “Podocytes are sensitive to fluid shear stress in vitro,” 291(4), F856-F865 (2006).
- [6] H. Dai, Q. Liu, and B. J. J. o. d. r. Liu, “Research progress on mechanism of podocyte depletion in diabetic nephropathy,” 2017, (2017).

- [7] M. Pourghasem, H. Shafi, and Z. J. C. j. o. i. m. Babazadeh, "Histological changes of kidney in diabetic nephropathy," 6(3), 120 (2015).
- [8] R. Maxson, and K. M. J. T. J. f. N. P. Lisenby, "Managing the Diabetic Kidney Patient," 14(7), 526-530 (2018).
- [9] K. V. Lemley, J. F. Bertram, S. B. Nicholas *et al.*, "Estimation of glomerular podocyte number: a selection of valid methods," 24(8), 1193-1202 (2013).
- [10] M. L. Graham, J. L. Janecek, J. A. Kittredge *et al.*, "The streptozotocin-induced diabetic nude mouse model: differences between animals from different sources," 61(4), 356-360 (2011).
- [11] O. Simon, R. Yacoub, S. Jain *et al.*, "Multi-radial LBP features as a tool for rapid glomerular detection and assessment in whole slide histopathology images," 8(1), 2032 (2018).
- [12] B. Lutnick, B. Ginley, D. Govind *et al.*, "An integrated iterative annotation technique for easing neural network training in medical image analysis," *Nature Machine Intelligence*, 1(2), 112 (2019).
- [13] R. E. Palmer, A. Kotsianti, B. Cadman *et al.*, "WT1 regulates the expression of the major glomerular podocyte membrane protein Podocalyxin," 11(22), 1805-1809 (2001).
- [14] B. Lutnick, B. Ginley, D. Govind *et al.*, "An integrated iterative annotation technique for easing neural network training in medical image analysis," *Nature Machine Intelligence*, 1(2), 112-119 (2019).
- [15] R. C. Gonzalez, and P. J. R. Wintz, Mass., Addison-Wesley Publishing Co., Inc., "Digital image processing(Book)," (13), 451 (1977).
- [16] K. Parvati, P. Rao, M. J. D. D. i. N. Mariya Das *et al.*, "Image segmentation using gray-scale morphology and marker-controlled watershed transformation," 2008, (2008).
- [17] B. J. C. S. H. P. Chazotte, "Labeling nuclear DNA using DAPI," 2011(1), pdb. prot5556 (2011).
- [18] G. R. Reddy, K. Kotlyarevska, R. F. Ransom *et al.*, "The podocyte and diabetes mellitus: is the podocyte the key to the origins of diabetic nephropathy?," 17(1), 32-36 (2008).
- [19] M. Nagata, Y. Yamaguchi, Y. Komatsu *et al.*, "Mitosis and the presence of binucleate cells among glomerular podocytes in diseased human kidneys," 70(1), 68-71 (1995).
- [20] N. K. Andeen, T. Q. Nguyen, F. Steegh *et al.*, "The phenotypes of podocytes and parietal epithelial cells may overlap in diabetic nephropathy," 88(5), 1099-1107 (2015).
- [21] M. Nagata, S. Shibata, M. Shigeta *et al.*, "Cyclin-dependent kinase inhibitors: p27kip1 and p57kip2 expression during human podocyte differentiation," 14(suppl_1), 48-51 (1999).
- [22] M. D. Hughson, W. E. Hoy, R. N. Douglas-Denton *et al.*, "Towards a definition of glomerulomegaly: clinical-pathological and methodological considerations," 26(7), 2202-2208 (2011).
- [23] J. Bariety, C. Mandet, G. S. Hill *et al.*, "Parietal podocytes in normal human glomeruli," 17(10), 2770-2780 (2006).
- [24] M. K. K. Niazi, A. V. Parwani, and M. N. J. T. L. O. Gurcan, "Digital pathology and artificial intelligence," 20(5), e253-e261 (2019).
- [25] A. Holzinger, B. Malle, P. Kieseberg *et al.*, "Towards the augmented pathologist: Challenges of explainable-ai in digital pathology," (2017).
- [26] A. J. I. i. m. Madabhushi, "Digital pathology image analysis: opportunities and challenges," 1(1), 7 (2009).